



**HAL**  
open science

## First-principles calculations to identify key native point defects in Sr<sub>4</sub>Al<sub>14</sub>O<sub>25</sub>

William Lafargue-Dit-Hauret, Camille Latouche, Mathieu Allix, Bruno Viana, Stéphane Jobic

► **To cite this version:**

William Lafargue-Dit-Hauret, Camille Latouche, Mathieu Allix, Bruno Viana, Stéphane Jobic. First-principles calculations to identify key native point defects in Sr<sub>4</sub>Al<sub>14</sub>O<sub>25</sub>. *Physical Chemistry Chemical Physics*, 2022, 24 (4), pp.2482-2490. 10.1039/d1cp03906g . hal-03547198

**HAL Id: hal-03547198**

**<https://hal.science/hal-03547198>**

Submitted on 7 Jul 2022

**HAL** is a multi-disciplinary open access archive for the deposit and dissemination of scientific research documents, whether they are published or not. The documents may come from teaching and research institutions in France or abroad, or from public or private research centers.

L'archive ouverte pluridisciplinaire **HAL**, est destinée au dépôt et à la diffusion de documents scientifiques de niveau recherche, publiés ou non, émanant des établissements d'enseignement et de recherche français ou étrangers, des laboratoires publics ou privés.

Cite this: DOI: 00.0000/xxxxxxxxxx

# First-principles calculations to identify key native point defects in $\text{Sr}_4\text{Al}_{14}\text{O}_{25}$ <sup>†</sup>

William Lafargue-Dit-Hauret,<sup>a</sup> Camille Latouche,<sup>a\*</sup> Mathieu Allix,<sup>b</sup> Bruno Viana,<sup>c</sup> and Stéphane Jobic<sup>a‡</sup>

Received Date

Accepted Date

DOI: 00.0000/xxxxxxxxxx

This article reports for the first time an in-depth *ab initio* computational study on intrinsic point defects in  $\text{Sr}_4\text{Al}_{14}\text{O}_{25}$  that serves as host lattice for numerous phosphors. Defect Formation Enthalpies (DFEs) and defect concentrations were computed considering the supercell approach for different oxygen atmospheres. The charge transition levels have been determined for several point defects in their thermodynamically stable state and their impact on the electronic structure of the ideal unfaulted material is discussed. Our simulations demonstrated that the formation of most of native point defects is energy intensive under oxygen-rich, -intermediate or -poor synthesis conditions, except for the oxygen vacancies under O-poor atmosphere.

<sup>a</sup> Université de Nantes, CNRS, Institut des Matériaux Jean Rouxel, IMN, F-44000 Nantes, France

<sup>b</sup> Conditions Extrêmes et Matériaux: Haute Température et Irradiation, CEMHTI, UPR 3079, CNRS, Université Orléans, Orléans 45071, France

<sup>c</sup> PSL Research University Chimie ParisTech, IRCP, CNRS, Paris, 75005 France

\* E-mail: camille.latouche@cnrs-imn.fr

\* E-mail: stephane.jobic@cnrs-imn.fr

† Electronic Supplementary Information (ESI) available: atomic positions, PDoS, charge density plots, position of interstitial atoms, corrections applied for defect formation enthalpies, PDoS for some point defects, defect formation enthalpies for each non-equivalent sites and different atmospheres, list of charge transition levels and evolution of defect concentrations vs synthesis temperature. See DOI: 10.1039/cXCP00000x/.

# 1 Introduction

$\text{Sr}_4\text{Al}_{14}\text{O}_{25}$  has become a popular material that has received much attention due to its capability to host transition elements or lanthanides to generate luminescence properties. Namely, a deep red emission with potential application in white lightening is observed when  $\text{Mn}^{4+}$  cations are used as activators.<sup>1-7</sup> In contrast,  $\text{Ce}^{3+}$  dopants induce a blue-green emission.<sup>8,9</sup> Moreover,  $\text{Mn}^{4+}, \text{Tb}^{3+}$  co-doped  $\text{Sr}_4\text{Al}_{14}\text{O}_{25}$  is a thermographic material for temperature imaging, as the emission color strongly changes due to the thermal quenching of the  $\text{Mn}^{4+}$  emission.<sup>10</sup>  $\text{Eu}^{2+}, \text{Eu}^{3+}$  co-doped  $\text{Sr}_4\text{Al}_{14}\text{O}_{25}$  also shows important color changes from 298 to 523 K.<sup>11</sup> In addition, a blue-green long lasting luminescence can be triggered by the co-insertion of  $\text{Eu}^{2+}$  and  $\text{Dy}^{3+}$  cations,<sup>12,13</sup> that may transform into a red luminescence if  $\text{Cr}^{3+}$  cations are added<sup>14,15</sup> Conversely, a blue afterglow is observed for  $\text{Tb}^{3+}$  dopants only.<sup>16</sup> Also, unintentional strontium and oxygen vacancies have been reported to possibly play a role in the luminescent phenomena.<sup>7,17-19</sup> Thus, a clear understanding of native point defects may be of prior importance before focusing on the role of dopants. To gain a deeper insight on these intrinsic species, theoretical studies are of particular interest. Indeed, *ab initio* methods can be used to estimate the formation energy of point defects, and to determine their impact on the electronic structure of the ideal material.<sup>20-31</sup> Surprisingly, from our knowledge, such kind of simulations have not been reported for the  $\text{Sr}_4\text{Al}_{14}\text{O}_{25}$  compound yet. Herein, we propose to fill this lack by characterizing more than 30 possible intrinsic point defects in this material and to identify the prominent expected ones versus specific synthesis conditions. In this article, we detail the computational approach used to investigate the electronic properties of the host compound and to estimate defect formation enthalpies and defect concentrations.

## 2 Methods

### 2.1 Calculations on the host structure

Spin polarized calculations based on the Density Functional Theory (DFT) have been carried out using the Projected Augmented Wave (PAW) method, as implemented within the VASP software.<sup>32-34</sup> The cutoff energy was set to 500 eV, and the exchange-correlation part was described with the meta-GGA SCAN approach.<sup>35</sup> Full geometry optimizations were performed on the  $\text{Sr}_4\text{Al}_{14}\text{O}_{25}$  unit-cell using a  $2 \times 6 \times 10$   $\Gamma$ -centered  $k$ -mesh and until forces were found below 10 meV/Å. The electronic band gap was extracted based on an accurate calculation considering a  $3 \times 9 \times 15$   $\Gamma$ -centered  $k$ -mesh. Accurate band gap was determined using PBE0<sup>36</sup> functional on the fully optimized SCAN structure referenced as PBE0@SCAN hereafter), considering a  $1 \times 2 \times 4$   $\Gamma$ -centered  $k$ -mesh.

### 2.2 Defect formation enthalpies and concentrations

Point defect calculations were carried out with the supercell approach. In that context, defect species are considered sufficiently diluted within the host material and no volume change associated to their insertion in the ideal material was taken into account.

A  $1 \times 1 \times 2$  supercell (172 atoms) was constructed based on the

fully optimized SCAN unit cell. Atomic positions were relaxed considering a  $1 \times 3 \times 2$   $\Gamma$ -centered  $k$ -mesh and until the convergence criterion on forces set to 0.02 eV/Å was reached. Accurate computation of total DFT energies was performed with a  $1 \times 4 \times 4$   $\Gamma$ -centered  $k$ -mesh.

One may estimate the Defect Formation Enthalpy (DFE)  $\Delta_f H^{D,q}$  of a defect  $D$  in a charge state  $q$  as a function of the chemical potential of the electronic reservoir (Fermi level)  $\mu_{E_F}$  according to:

$$\Delta_f H^{D,q}(\mu_{E_F}) = E_{DFT}^{D,q} - E_{DFT}^{host} + q \left( E_{VBM}^{host} + \mu_{E_F} \right) + \sum_i n_i \mu_i + E_{corr} \quad (1)$$

where  $E_{DFT}^{D,q}$  is the total DFT energy of the faulted supercell,  $E_{DFT}^{host}$  is the total DFT energy of the ideal supercell,  $E_{VBM}^{host}$  is the valence band maximum (VBM) of the host material which sets the origin of  $\mu_{E_F}$ ,  $n_i$  is the number of atoms of the  $i$ th specie added ( $n_i < 0$ ) or removed ( $n_i > 0$ ) from the ideal material,  $\mu_i$  is the chemical potential of the  $i$ th species defined as  $\mu_i^0 + \Delta\mu_i$ , *i.e.* the sum of the standard chemical potential  $\mu_i^0$  and the deviation  $\Delta\mu_i$  from this reference.  $E_{corr}$  corresponds to various corrections of spurious effects introduced by the supercell approach, *i.e.* the so-called band-edges shift, Perturbed Host State (commonly abbreviated PHS), potential alignment, Moss-Burstein and Makov-Payne corrections (see Section I in SI for more details).

For a defect  $D$ , the Fermi level position at which DFEs of charge states  $q$  (*i.e.*  $\Delta_f H^{D,q}$ ) and  $q'$  (*i.e.*  $\Delta_f H^{D,q'}$ ) are equivalent and it corresponds to the so-called charge transition level  $\varepsilon(q/q')$  formulated as:

$$\varepsilon(q/q') = - \frac{\Delta_f H^{D,q'}(\mu_{E_F} = 0) - \Delta_f H^{D,q}(\mu_{E_F} = 0)}{q' - q} \quad (2)$$

Practically, for  $\mu_{E_F}$  equals to  $\varepsilon(q/q')$ , the  $D^q$  and  $D^{q'}$  species coexist in identical concentrations. For  $\mu_{E_F}$  higher (lower) than  $\varepsilon(q/q')$ , defect  $D$  with the charge state  $q'$  ( $q$ ) will be predominant on defect  $D$  with charge state  $q$  ( $q'$ ). Moreover, to estimate point defect concentrations at a given crystal growth temperature  $T_{gr}$  (in given synthesis conditions), one may solve the charge neutrality equation expressed in Equation 4 by determining iteratively the Fermi level at crystal growth  $E_F^{gr}$ . To do so, one assumes the faulted structure is quenched at room temperature, and defect concentrations are described within the Boltzmann limit:

$$n_{D,q}(E_F^{gr}) \approx \frac{N}{\Omega} \cdot \exp\left(-\frac{\Delta_f H^{D,q}(E_F^{gr})}{k_B T_{gr}}\right) \quad (3)$$

where  $N$  is the number of sites,  $\Omega$  the volume,  $k_B$  is the Boltzmann constant. The charge neutrality equation expresses as:

$$-n_{e^-}(E_F) + n_{h^+}(E_F) + \sum_D \sum_{q_i \in q_D} q_i \cdot n_{D,q_i}(E_F) = 0 \quad (4)$$

where  $n_{e^-}$  and  $n_{h^+}$  correspond to the free electrons and holes, respectively (more details are given in SI Section II). Defect created at  $T_{gr}$  are supposed to be maintained at RT after quenching. For each defect, the concentration remains constant but their charge

state may change (since the Fermi level moves with temperature).

All defect post-treatments presented above were performed using the PyDEF 2.0 software.<sup>37,38</sup>

## 3 Results

### 3.1 Ideal crystal

$\text{Sr}_4\text{Al}_{14}\text{O}_{25}$  crystallizes in the  $Pm\bar{m}a$  space group (#51).<sup>39</sup> The crystal structure is depicted in Figure 1 with labelling of Sr and Al symmetry non-equivalent atoms (more details on symmetrically non-equivalent sites are given in SI Section III). The structure can be decomposed into layers of  $\text{Al}_4\text{O}_{12}$  formula, hereafter labelled  $^{2/\infty}[\text{Al}_4\text{O}_{12}]$  (see Figure 1a) made of edge sharing  $\text{AlO}_6$  octahedra (where Al = Al(4), Al(5) and Al(6)) and bidimensional blocks of  $\text{Al}_{10}\text{O}_{23}$  formulae, hereafter labelled  $^{2/\infty}[\text{Al}_{10}\text{O}_{23}]$  (see Figure 1b) made of corner sharing  $\text{AlO}_4$  tetrahedra (where Al = Al(1), Al(2) and Al(3)). Layers and blocks condense via four  $[\text{Al}(2)\text{O}_4]$  tetrahedra capping head to head  $^{2/\infty}[\text{Al}_4\text{O}_{12}]$  layers (see Figure 1c) at the level of empty octahedral sites. The so-defined three dimensional  $[\text{Al}_{14}\text{O}_{25}]$  aluminate framework entraps 10- and 7- coordinated strontium atoms (Sr(1) and Sr(2), respectively), to balance charges. As shown in Figure 1, this structure also presents empty spaces which could be filled by interstitial atoms. Due to the abundance of these interstitial sites, only three of them were considered during our point defect study: i) the  $i(1)$  site (pink spheres in Figure 1) which initially sits within a channel oriented along the  $c$  axis of the  $^{2/\infty}[\text{Al}_{10}\text{O}_{23}]$  blocks (*i.e.* perpendicular to the  $^{2/\infty}[\text{Al}_4\text{O}_{12}]$  layers) defined by Al(1), Al(2) and Sr(2) atoms, ii) the  $i(2)$  site (yellow sphere in Figure 1) initially located into a cage defined by Al(1), Al(3) and Sr(1) atoms, and iii) the  $i(3)$  site (orange spheres in Figure 1) initially located into empty octahedral sites of the  $^{2/\infty}[\text{Al}_4\text{O}_{12}]$  layers (coordinates are provided in SI Section III).

Full geometry relaxations using the SCAN functional lead to  $a = 24.739 \text{ \AA}$ ,  $b = 8.476 \text{ \AA}$ ,  $c = 4.876 \text{ \AA}$ , agreeing well with experimental values reported to be  $a = 24.785(1) \text{ \AA}$ ,  $b = 8.487(2) \text{ \AA}$ ,  $c = 4.886(1) \text{ \AA}$ .<sup>39</sup> The electronic bandstructure determined at the SCAN level (see Figure 2) indicates an indirect band gap (following already reported WC1PBE calculations<sup>40</sup>) of 4.60 eV between the Valence Band Maximum (VBM) located at the  $Y$  point and the Conduction Band Minimum (CBM) at the  $\Gamma$  point. The upper part of the valence band consists in flat states isolated from the main part of the valence band. We estimated the effective mass for holes with the well-known curvature fitting method, and found  $m_{h^+}^*/m_0 = 5.21$  for the  $T \rightarrow Y$   $k$ -points path. In contrast, the bottom of the conduction band looks much less localized, and an electron effective mass  $m_{e^-}^*/m_0$  of 0.46 is calculated considering the  $R \rightarrow \Gamma$   $k$ -points path.

The analysis of the partial Density of States (pDOS) depicted in Figure 2 (see SI Section IV for a broader outlook of pDOS) reveals that the valence band mainly built upon O  $2p$  states, while Sr atoms predominantly contribute to the bottom of the conduction band. Let us notice that the distinguishable band on top of the valence band is associated specifically to orbitals of O(5) atoms that can almost be regarded as lone pairs (see SI Section IV for pDOS of each symmetrically non-equivalent site, and SI Section

Point	$\mu_{\text{Sr}} (\Delta\mu_{\text{Sr}})$	$\mu_{\text{Al}} (\Delta\mu_{\text{Al}})$	$\mu_{\text{O}} (\Delta\mu_{\text{O}})$
A	-29.35 (-7.06)	-16.50 (-8.78)	-6.02 (0.00)
B	-29.03 (-6.74)	-16.59 (-8.86)	-6.02 (0.00)
C	-23.52 (-1.23)	-7.76 (-0.03)	-11.85 (-5.83)
D	-23.20 (-0.91)	-7.84 (-0.11)	-11.86 (-5.84)

**Table 1** Chemical potential values (in eV) estimated in SCAN for extreme limit synthesis conditions. Deviations with respect to standard are given between brackets.

V for a representation of the charge density associated to the top of the valence band). Formally, this O(5) atomic site is unique in the sense that the  $[\text{O}(5)\text{Al}_3\text{Sr}]$  environment is highly distorted with an oxygen atom connected only to three aluminum atoms in octahedral site ( $^{2/\infty}[\text{Al}_4\text{O}_{12}]$  layer), the other oxygens being bounded to one or more aluminum atoms in tetrahedral sites.

The computation of reliable defect formation enthalpies requires a good estimation of the band gap, the SCAN value (4.60 eV) being far from the experimental one measured at 6.20-6.30 eV.<sup>41,42</sup> Based on the fully relaxed SCAN structure, this quantity was determined using hybrid approaches. We found  $E_g(\text{PBE0@SCAN}) = 6.37 \text{ eV}$ , not far from already reported WC1PBE hybrid results<sup>40</sup> and in line with the work of some of us which predicted more reliable large band gaps with the PBE0 approach.<sup>43</sup> Thus, this PBE0 result will be considered hereafter to readjust calculations carried out with the SCAN functional.

### 3.2 Stability domain

To investigate the impact of synthesis conditions on the formation of native point defects, the stability domain (domains/conditions of existence/growth of the pure phase) of the  $\text{Sr}_4\text{Al}_{14}\text{O}_{25}$  material was determined in terms of chemical potentials as presented in Equation 1. To do so, we computed the formation enthalpy of 13 competitive phases susceptible to appear during the material synthesis (see Figure 3). Based on a numerical procedure detailed in Ref 44, we extracted the extreme limit synthesis conditions, evidenced by cyan stars in Figure 3 and listed in Table 1.

We distinguished two neighboring synthesis condition limits for extreme O-rich atmosphere (*e.g.* in pure oxygen at ambient pressure) at A and B points and extreme O-poor atmosphere (*e.g.* in evacuated sealed silica tube) at C and D points. For the sake of clarity, we restrain hereafter our reasoning to i) the extreme O-rich atmosphere at the A point of coordinates  $(\Delta\mu_{\text{Sr}}, \Delta\mu_{\text{Al}}, \Delta\mu_{\text{O}}) = (-7.06, -8.78, 0.00) \text{ eV}$ , ii) the extreme O-poor atmosphere at the D point of coordinates  $(-0.91, -0.11, -5.84) \text{ eV}$ , and iii) an intermediate conditions corresponding to the barycenter of the four points of coordinates  $(-3.98, -4.45, -2.92) \text{ eV}$ .

Based on the expression of the formation enthalpy of the strontium aluminate compound:

$$\Delta_f H(\text{Sr}_4\text{Al}_{14}\text{O}_{25}) = 4\Delta\mu_{\text{Sr}} + 14\Delta\mu_{\text{Al}} + 25\Delta\mu_{\text{O}} \quad (5)$$

we estimated  $\Delta_f H(\text{Sr}_4\text{Al}_{14}\text{O}_{25}) = -151.07 \text{ eV}$ , never reported yet. For comparison, we estimated  $\Delta_f H(\text{Al}_2\text{O}_3) = -17.55 \text{ eV}$  (-17.37 eV experimentally<sup>45</sup>) and  $\Delta_f H(\text{SrO}) = -7.06 \text{ eV}$  (-6.14 eV experimentally<sup>46</sup>), found in good agreement with the experimental

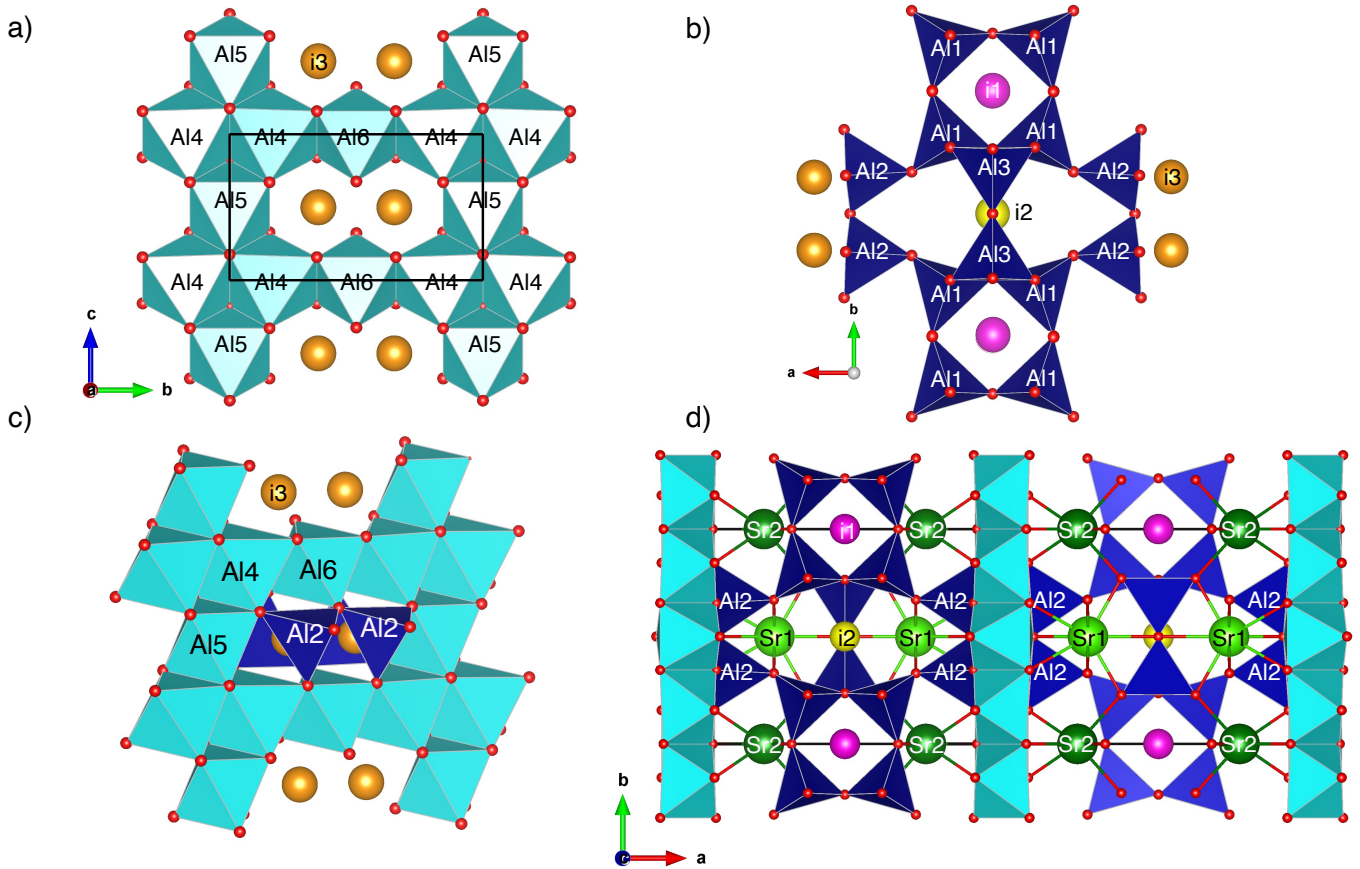


**Fig. 1** a)  $^{2/\infty}$   $[\text{Al}_4\text{O}_{12}]$  layer running in the (100) plane; b)  $^{2/\infty}$   $[\text{Al}_{10}\text{O}_{23}]$  blocks running in the (100) plane and connecting  $^{2/\infty}$   $[\text{Al}_4\text{O}_{12}]$  layers along the  $a$  axis; c) Condensation of  $[\text{Al}(2)\text{O}_4]$  tetrahedra on a  $^{2/\infty}$   $[\text{Al}_4\text{O}_{12}]$  layer; d)  $\text{Sr}_4\text{Al}_{14}\text{O}_{25}$  3D-structure. Sr(1) and Sr(2) sites are distinguished by dark and light green spheres, respectively. Al(Oh) and Al(Td) environments are identified by dark blue and cyan polyhedra, respectively. Oxygen atoms are showed by red spheres. Labelling of oxygen atoms is given in SI Section III. Initial positions (before relaxation) used for interstitial defects  $i(1)$ ,  $i(2)$  and  $i(3)$  are shown by pink, yellow and orange spheres, respectively.

data.

### 3.3 Defect Formation Enthalpies

Defect formation enthalpies (DFEs) were estimated for different intrinsic point defects. All symmetrically non-equivalent crystallographic sites were considered for atomic vacancies and antisites. Due to the lack of information regarding interstitial species, the three aforementioned positions were chosen (see SI Section VI for reduced coordinates of initial positions). More precisely, the interstitial sites  $i(1)$  and  $i(2)$  were occupied by Sr, Al and O atoms. Specifically regarding the  $i(3)$  position into  $^{2/\infty}$   $[\text{Al}_4\text{O}_{12}]$  layers, we restricted the study to its occupancy by an Al atom, the most favourable atomic species regarding the octahedral chemical environment formed by six oxygen atoms and which presents a similar volume as the  $\text{AlO}_6$  neighboring ones.

The local structural distortions induced by the presence of point defects were taken into account in the estimation of DFEs through preliminary atomic positions relaxation. For instance, in the case of  $V_{\text{Sr}(1)}$  species (e.g. the removal of an Sr(1) entity), we observed that the neighboring O sites may move away of about 0.2 Å due to the coordination loss. On the contrary, the neighboring Al are less impacted. The resulting DFEs are schematically summarized

in Figure 4 (see SI Section VII for more details on DFEs at each atmosphere of synthesis).

Let us have a look at the impact of synthesis conditions, for which DFEs may significantly change. Under an extreme O-rich (oxidized) atmosphere, the DFEs for  $V_{\text{Sr}}$  species cross the line of zero formation enthalpy at  $\mu_{E_F} = 3.04$  eV (namely for  $V_{\text{Sr}(1)}$ ), far from the CBM. In the case where  $\mu_{E_F}$  would be found above this limit,  $V_{\text{Sr}}$  vacancies would be spontaneously created and would destabilize the system with appearance of a Sr-poor phase at the expense of  $\text{Sr}_4\text{Al}_{14}\text{O}_{25}$ . The lower limit of allowed  $\mu_{E_F}$  values is set by  $V_{\text{O}}$  species close to the VBM, i.e. at 0.14 eV for  $V_{\text{O}(5)}$ . In this dopability domain, i.e. the  $\mu_{E_F}$  bounded domain where  $\text{Sr}_4\text{Al}_{14}\text{O}_{25}$  is stable, lowest DFEs were observed for  $V_{\text{O}}$ ,  $V_{\text{Sr}}$ ,  $\text{Sr}_i$  and  $\text{O}_i$  species, while  $V_{\text{Al}}$ ,  $\text{Sr}_{\text{Al}}$  or even  $\text{Al}_{\text{Sr}}$  entities present higher DFEs and should not be formed. Regarding the O-intermediate synthesis condition, the  $V_{\text{O}}$  and  $V_{\text{Sr}}$  species also limit the dopability domain which is now centered between 1.59 and 4.58 eV. The  $V_{\text{Sr}}$ ,  $\text{Sr}_i$  and  $V_{\text{O}}$  show the lowest DFEs in this  $\mu_{E_F}$  range, while the formation of  $\text{Al}_i$ ,  $\text{Sr}_{\text{Al}}$  or  $V_{\text{Al}}$  is strongly disfavoured. In the case of O-poor (reduced) synthesis conditions, the dopability region is still set by the same defects (i.e.  $V_{\text{O}}$  and  $V_{\text{Sr}}$ ) between 3.05 and 5.96 eV. Here, the formation of oxygen vacancies is particularly

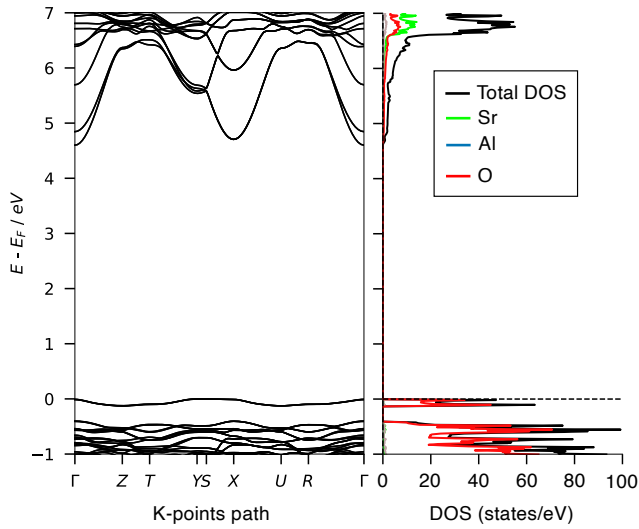


**Fig. 2** (left) Electronic bandstructure computed at the SCAN level. High symmetry  $k$ -points are  $\Gamma$  (0, 0, 0), Z (0, 0,  $\frac{1}{2}$ ), T (0,  $\frac{1}{2}$ ,  $\frac{1}{2}$ ), Y (0,  $\frac{1}{2}$ , 0), S ( $\frac{1}{2}$ ,  $\frac{1}{2}$ , 0), X ( $\frac{1}{2}$ , 0, 0), U ( $\frac{1}{2}$ , 0,  $\frac{1}{2}$ ) and R ( $\frac{1}{2}$ ,  $\frac{1}{2}$ ,  $\frac{1}{2}$ ). (right) Partial Density of States (pDOS) projected on atoms. Sr, Al and O contributions are evidenced by green, blue and red colors, respectively.

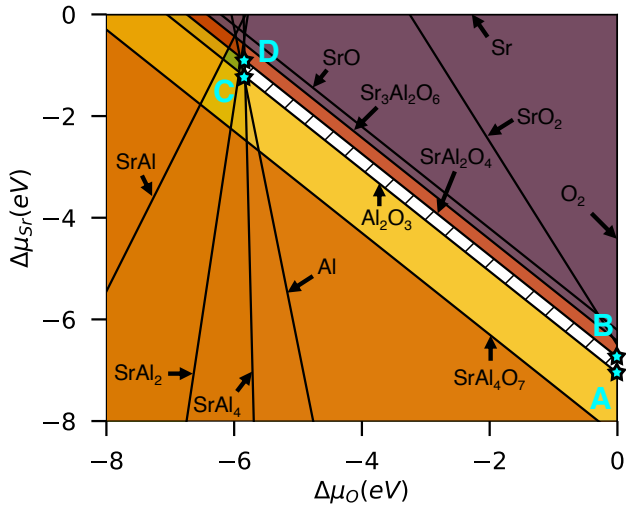


**Fig. 3** Stability domain of the  $\text{Sr}_4\text{Al}_{14}\text{O}_{25}$  phase with respect to chemical potential deviations  $\Delta\mu_{\text{Sr}}$  and  $\Delta\mu_{\text{O}}$ . For more clarity, the domain of  $\text{Sr}_4\text{Al}_{14}\text{O}_{25}$  existence is represented by a white hatched area, while the one of competing phases is colored. Extreme limit synthesis conditions are evidenced by cyan stars and are detailed in Table 1. Arrows point toward the stability limit of competing phases.

favorable with DFEs lower than 1.69 eV in this domain.

Clearly, two groups of oxygen vacancies are distinguishable: i) one with DFEs for  $q = 0$  higher than 1.38 eV, 4.29 eV and 7.21 eV in O-poor, O-intermediate and O-rich atmosphere, respectively, gathering oxygen sites triply coordinated to Al atoms (i.e.  $V_{O(1)}$ ,  $V_{O(4)}$ ,  $V_{O(5)}$ ,  $V_{O(6)}$  and  $V_{O(8)}$ ), most of them belonging to  $2/\infty$   $[\text{Al}_4\text{O}_{12}]$  layers, and ii) one with slightly lower DFEs which consists in oxygen sites coordinated to two Al atoms (i.e.  $V_{O(2)}$ ,  $V_{O(3)}$ ,  $V_{O(7)}$  and  $V_{O(9)}$ ).

The positions of the charge transition levels estimated from

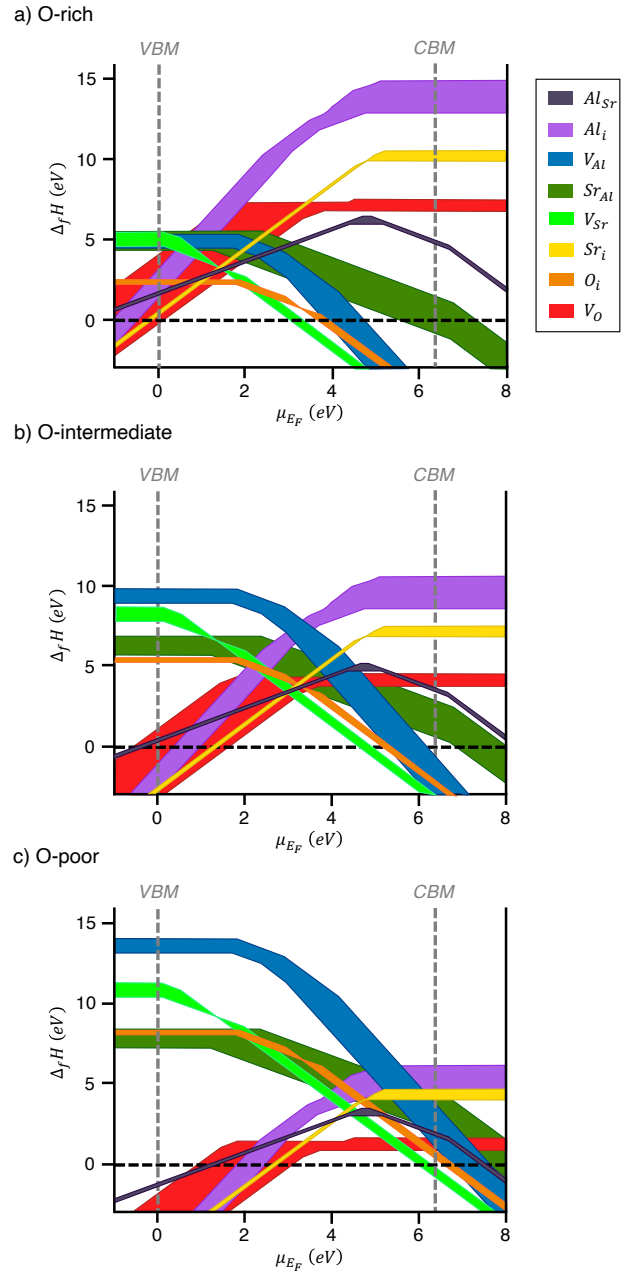


**Fig. 4** Schematic representation of defect formation enthalpies vs  $\mu_{E_F}$  for O point defects under a) O-rich, b) O-intermediate and c) O-poor atmospheres. Colored regions evidence minimum and maximum DFEs for the different defect species, independently of the crystallographic site. The exact calculated DFEs for each crystallographic sites are given in SI Section VII.

DFEs are reported in Figure 5 for Sr-based species, Figure 6 for Al-based species and Figure 7 for O-based species (all values are summarized in SI Section IX).

In the case of Sr-based defects, both interstitial strontium atoms at  $i(1)$  and  $i(2)$  sites introduce transition levels located between 1.2 and 1.9 eV below the CBM. Independently of DFEs, the charge state  $q = +2$  (i.e. formally  $\text{Sr}^{2+}$  cations) is stable under the three synthesis conditions. In contrast,  $q = +1$  (i.e. formally  $\text{Sr}^+$ ) and 0 (i.e. formally  $\text{Sr}^0$ ) are only accessible under

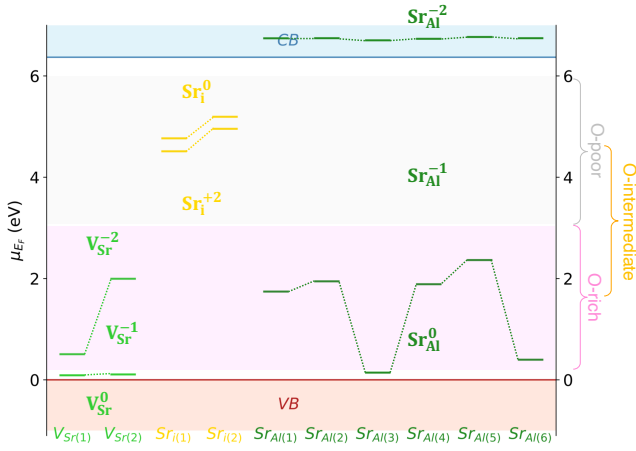


**Fig. 5** Charge transition levels for Sr-based native point defects in  $\text{Sr}_4\text{Al}_{14}\text{O}_{25}$ . Values are listed in SI Table S2. Dopability domains in O-rich, O-intermediate and O-poor conditions are also given (see text for values).

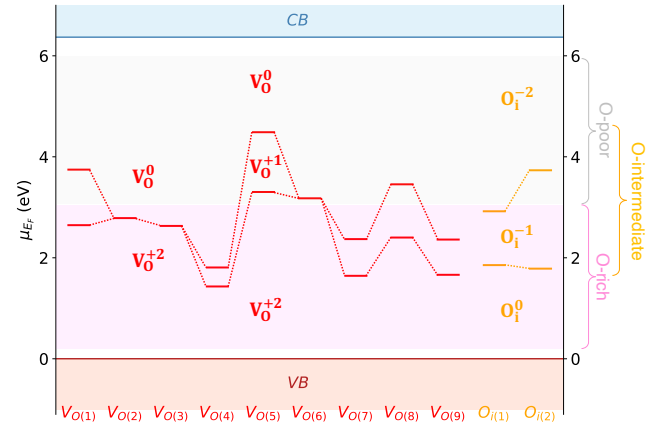


**Fig. 7** Charge transition levels for O-based native point defects in  $\text{Sr}_4\text{Al}_{14}\text{O}_{25}$ . Values are listed in SI Table S4. Dopability domains in O-rich, O-intermediate and O-poor conditions are also given (see text for values).

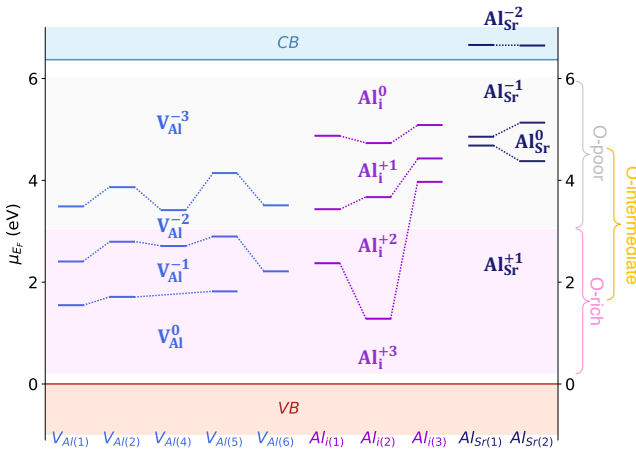


**Fig. 6** Charge transition levels for Al-based native point defects in  $\text{Sr}_4\text{Al}_{14}\text{O}_{25}$ . Values are listed in SI Table S3. Dopability domains in O-rich, O-intermediate and O-poor conditions are also given (see text for values).

O-intermediate and O-poor conditions. On the other side, strontium vacancies were found to create shallow acceptor states at the top of the VBM by positioning  $\epsilon(0/-1)$  levels at  $\sim 0.1$  eV for both Sr(1) and Sr(2) sites. Also, the  $\epsilon(-1/-2)$  level is estimated near the VBM ( $\sim 0.5$  eV) for Sr(1) site (10-coordinated), while it appears at 2 eV for a vacancy in Sr(2) site (7-coordinated). Whatever the synthesis conditions are, only the  $q = -2$  state (namely the removing of one  $\text{Sr}^{2+}$ ) shows sufficiently low DFEs to potentially appear. For  $\text{Sr}_{\text{Al}}$  antisites, only the substitution of  $\text{Al}^{3+}$  by  $\text{Sr}^{2+}$  may be observed for O-poor atmospheres, while all the  $\text{Sr}_{\text{Al}}^0$  and  $\text{Sr}_{\text{Al}}^{-1}$  species may appear under O-rich conditions. For the O-intermediate condition, the  $\epsilon(0/-1)$  charge transition of the  $\text{Sr}_{\text{Al}(1)}$ ,  $\text{Sr}_{\text{Al}(2)}$ ,  $\text{Sr}_{\text{Al}(4)}$  and  $\text{Sr}_{\text{Al}(5)}$  defects are lying in the lower part of the  $\mu_{\text{E}_f}$  allowed range, while the  $\text{Sr}_{\text{Al}(3)}^0$  and  $\text{Sr}_{\text{Al}(6)}^0$  species cannot be created. At  $q = 0$ , the lowest DFEs are observed for Al(1) sites, *i.e.* aluminum sites that surround the empty channels. In terms of the position of  $\epsilon(0/-1)$  acceptor levels, one may dis-

tinguish i)  $\text{Sr}_{\text{Al}}$  at the tetrahedral Al(3) site with the transition level at 0.14 eV (Al(3), constituting also the channels), ii)  $\text{Sr}_{\text{Al}}$  at the octahedral Al(6) site with the transition level at 0.40 eV (within the  $^{2/\infty}[\text{Al}_4\text{O}_{12}]$  layers) and iii)  $\text{Sr}_{\text{Al}}$  at the other Al sites with the transition levels located between 1.74 and 2.37 eV. It is worth noticing that most of these charged defects present high DFEs for the three atmospheres; they are consequently difficult to form within  $\text{Sr}_4\text{Al}_{14}\text{O}_{25}$ .

Regarding the Al-based point defects, most of transition levels are located far from the VBM and the CBM. For example, the ones associated to interstitials ( $\text{Al}_i$ ) were found well separated from each other between 1.28 and 5.09 eV above the VBM. Concerning the  $\text{Al}_{\text{Sr}}$  antisites,  $\text{Sr}^{2+}$  species are preferentially substituted by  $\text{Al}^{3+}$  under O-intermediate and O-rich conditions, the position of the antisite levels  $\epsilon(+1/0)$  being located at 1.69 and 1.99 eV below the CBM for  $\text{Al}_{\text{Sr}(1)}$  and  $\text{Al}_{\text{Sr}(2)}$ , respectively. These levels and also the  $\epsilon(0/-1)$  ones found at 1.23-1.51 eV below the CBM are located within the O-poor dopability domain, which implies defects at charge states  $q = +1, 0$  and  $-1$  may be created under such atmospheres, while  $q = -2$  defects are unstable. For  $\text{V}_{\text{Al}}$  vacancies, the charged defects generate deep levels distributed between 1.55 and 4.14 eV above the VBM. One may emphasize that i) charged defects for  $\text{V}_{\text{Al}(3)}$  species at  $q \neq -3$  were not successfully stabilized in spite of our efforts to force the system to converge (not represented in Figure 6), and ii)  $\text{V}_{\text{Al}(4)}^0$  and  $\text{V}_{\text{Al}(6)}^0$  entities are not stable (whatever the synthesis conditions are) due to  $\epsilon(0/-1)$  located at 1.88 and 2.21 eV below the VBM, respectively. This result shows that these Al centered polyhedra sites constitute too stabilizing building blocks for the structure to be removed. Moreover, different charge transition levels may be accessed by changing the synthesis conditions: i) O-rich conditions enables to recover the  $\epsilon(0/-1)$  and  $\epsilon(-1/-2)$  levels, ii) the  $\epsilon(-1/-2)$  and  $\epsilon(-2/-3)$  levels may be found under the O-intermediate atmosphere, and iii) the  $\epsilon(-2/-3)$  may be reached under O-poor conditions.

In the case of O-based defects, the levels of interstitials ( $\text{O}_i$ ) are

sitting in the mid-gap region, *i.e.* between 1.79 and 3.73 eV, so mainly accessible under O-intermediate and O-rich atmosphere while almost only  $q = -2$  states may be stabilized under O-poor conditions. Regarding  $V_O$  vacancies, the position of  $\varepsilon(q/q')$  levels may significantly differ with the crystallographic site, as evidenced by their distribution between 1.43 and 4.49 eV from the VBM. Thus, depending on the localization of the  $V_O$  defect, different energy windows are targeted. Levels are so deep that most of the charged defects may only be formed under O-intermediate or O-rich conditions to lie in the dopability domain.

### 3.4 Defect Concentrations

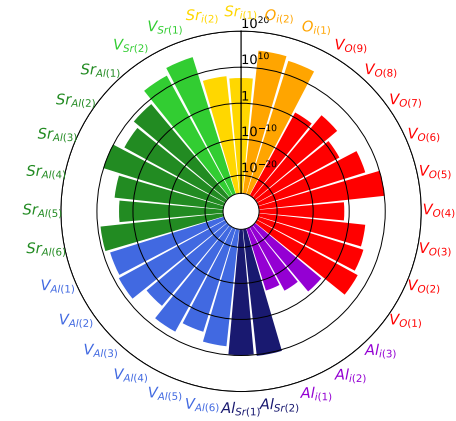
Based on the aforementioned DFEs quantities, we estimated defect concentrations with respect to the growth temperature  $T_{gr}$  within the Boltzmann approximation (see Equation 3). Experimentally, solid state synthesis have been reported at 1300-1500°C ( $\approx 1580-1780$  K).<sup>47-50</sup> Results are depicted in Figure 8 for  $T_{gr} = 1600$  K in the three synthesis conditions and the numerical values are reported in SI Section X. A wide range of temperature (100-1800 K) is also presented to show the physical trend.

Under O-rich atmosphere, small native defect concentrations are observed even at very high temperatures (*i.e.*  $< 7.2 \times 10^{14}$  cm<sup>-3</sup>). For  $T_{gr} = 1600$  K ( $E_F^{gr} = 1.98$  eV), strontium vacancies ( $[V_{Sr(1)}] = 7.2 \times 10^{14}$  cm<sup>-3</sup> and  $[V_{Sr(2)}] = 8.3 \times 10^{12}$  cm<sup>-3</sup>) and oxygen interstitials ( $[O_{i(2)}] = 7.0 \times 10^{14}$  cm<sup>-3</sup> and  $[O_{i(1)}] = 5.8 \times 10^{13}$  cm<sup>-3</sup>) appear as the most concentrated defects. For O-intermediate growth conditions, all defects show very small concentrations. As evidenced at  $T_{gr} = 1600$  K ( $E_F^{gr} = 3.10$  eV), the largest values are reached by  $V_{Sr(1)}$  ( $1.8 \times 10^{12}$  cm<sup>-3</sup>) and  $V_{O(5)}$  ( $1.4 \times 10^{12}$  cm<sup>-3</sup>), the others being lower than  $6 \times 10^{10}$  cm<sup>-3</sup>. In the case of O-poor atmosphere, oxygen vacancies appear (as expected) as the predominant point defect even for low growth temperatures. As discussed for DFEs, two groups were distinguished in that case, i) the most concentrated species  $V_{O(2)}$ ,  $V_{O(3)}$ ,  $V_{O(7)}$  and  $V_{O(9)}$  doubly bounded to Al atoms, and ii) the smallest concentrated species  $V_{O(1)}$ ,  $V_{O(4)}$ ,  $V_{O(5)}$ ,  $V_{O(6)}$  and  $V_{O(8)}$  triply bounded to Al atoms. For  $T_{gr} = 1600$  K ( $E_F^{gr} = 4.49$  eV), we calculated for the former group values about  $1.7-7.8 \times 10^{18}$  cm<sup>-3</sup>, and for the second group concentrations about  $1.9 \times 10^{16}-3.6 \times 10^{17}$  cm<sup>-3</sup>. These concentrations are much higher than all other defects ( $< 3 \times 10^{12}$  cm<sup>-3</sup>). Let us mention that oxygen vacancies will be preferentially located within  ${}^{2/\infty} [Al_{10}O_{23}]$  blocks rather than  ${}^{2/\infty} [Al_4O_{12}]$  layers.

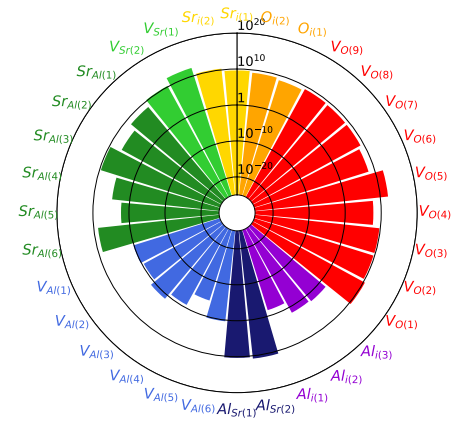
## 4 Discussion

From our computational study, one can briefly conclude on the fact that most of native point defects in  $Sr_4Al_{14}O_{25}$  cost a lot of energy to be created. Under an extreme O-rich and O-intermediate atmosphere of synthesis, defects are hardly created as depicted by calculated concentrations lower than  $10^{15}$  cm<sup>-3</sup> for  $T_{gr} = 1600$  K. Under extreme O-poor conditions, only oxygen vacancies may be easily formed with concentrations reaching  $10^{17}-10^{18}$  cm<sup>-3</sup> (per oxygen crystallographic positions). Also, we evidenced that Al- and O-based defect species present transition levels deeply located within the band gap, while Sr-

a) O-rich



b) O-intermediate



c) O-poor

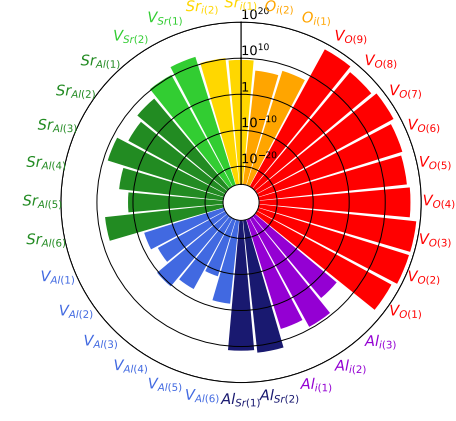


**Fig. 8** Calculated defect concentrations (in cm<sup>-3</sup>) at the SCAN level for  $Sr_4Al_{14}O_{25}$  prepared at  $T_{gr} = 1600$  K under a) O-rich, b) O-intermediate and c) O-poor atmospheres typically,  $10^{10}$  defects/cm<sup>-3</sup> corresponds to 1 defect every  $10^{14}$  Å<sup>3</sup>, *i.e.* approximately  $10^{-11}$  defect per  $Sr_4Al_{14}O_{25}$  unit cell or per  $Sr_8Al_{28}O_{50}$  formulae.

based vacancies ( $V_{Sr}$ ) and antisites ( $Sr_{Al}$ ) may create shallow acceptor states.

Many experimental investigations reported various luminescent properties of  $Sr_4Al_{14}O_{25}$  when doped with transition metals or lanthanides.<sup>1,7,9,13,19</sup> Indeed, this doped material may appear as appealing for industrial lighting applications. Among

the most promising discoveries is the red luminescence of  $\text{Sr}_4\text{Al}_{14}\text{O}_{25}:\text{Mn}^{4+}$ ,<sup>1</sup> possibly used as a key ingredient to improve the color rendering of the white light-emitting diode (WLED) technologies based on the InGaN/YAG:Ce<sup>3+</sup> approach. Peng *et al.*<sup>4</sup> suggested that under a UV or blue light excitation, Mn<sup>4+</sup> is excited from the ground state <sup>4</sup>A<sub>2</sub> to the excited state <sup>4</sup>T<sub>1</sub>. After a non-radiative transfer to the <sup>2</sup>E state, the return to the <sup>4</sup>A<sub>2</sub> state is accompanied by a red emission. Interestingly, another experimental study concluded on the enhancement of this red luminescence intensity by the increase of oxygen vacancies that would play the role of "sensitizers" towards Mn<sup>4+</sup> activators.<sup>7</sup> Such a scenario might be envisioned based on our simulations with transition levels dispersed within the band gap.

In the general case of (Eu,Dy)-doped strontium aluminates, various mechanisms have been proposed to explain the origin of their observed long lasting luminescence.<sup>51–54</sup> In the specific case of co-doped  $\text{Sr}_4\text{Al}_{14}\text{O}_{25}$ , an important argument in the debate has been brought by a recent experimental investigation which demonstrated the operating  $\text{Eu}^{2+} + \text{Dy}^{3+} \rightarrow \text{Eu}^{3+} + \text{Dy}^{2+}$  charge transfer under excitation and the role of Dy<sup>3+</sup> as electron traps.<sup>13</sup> Here, by exploring intrinsic point defects, our DFT calculations established that transition levels are relatively far from the CBM (*i.e.* more than 1 eV), which in a sense confirms the spectator role of native defects in this particular luminescence phenomenon.

## 5 Conclusion

To summarize, we conducted for the first time *ab initio* calculations on the  $\text{Sr}_4\text{Al}_{14}\text{O}_{25}$  compound to simulate intrinsic point defects. More concretely, we extracted defect formation enthalpies and estimated defect concentrations with respect to the crystal growth temperature. We showed that most of native defects are expected in moderate concentrations (lower than 10<sup>15</sup> cm<sup>-3</sup>) under O-rich and O-intermediate conditions, while oxygen vacancies are present in O-poor atmospheres (up to 8×10<sup>18</sup> cm<sup>-3</sup>). Also, we reported on the impact of the presence of defects on the ideal  $\text{Sr}_4\text{Al}_{14}\text{O}_{25}$  electronic structure with positioning of transition levels associated to defects in different charged states. This may serve to discuss physical properties of the undoped and doped material.

## Conflicts of interest

There are no conflicts to declare.

## Acknowledgements

This work was performed using HPC resources from GENCI-TGCC (Grant 2020-A0080911491) and CCIPL (Centre de Calculs Intensifs des Pays de la Loire). W.L.-D.-H. particularly thanks the financial support by the ANR-18-CE08-0012 PERSIST project of the French National Research Agency and the CNRS. Crystal structures were represented using the VESTA software.<sup>55</sup>

## Notes and references

1 M. Peng, X. Yin, P. A. Tanner, C. Liang, P. Li, Q. Zhang and J. Qiu, *Journal of the American Ceramic Society*, 2013, **96**, 2870–2876.

- 2 L. Chen, X. Deng, E. Zhao, X. Chen, S. Xue, W. Zhang, S. Chen, Z. Zhao, W. Zhang and T.-S. Chan, *Journal of Alloys and Compounds*, 2014, **613**, 312–316.
- 3 L. Chen, S. Xue, X. Chen, A. Bahader, X. Deng, E. Zhao, Y. Jiang, S. Chen, T.-S. Chan, Z. Zhao and W. Zhang, *Materials Research Bulletin*, 2014, **60**, 604–611.
- 4 M. Peng, X. Yin, P. A. Tanner, M. G. Brik and P. Li, *Chemistry of Materials*, 2015, **27**, 2938–2945.
- 5 Y.-d. Xu, X.-d. Peng, L. Wang, M. Shi, Y. Zhang, Q. Wang, S. Qi and N. Ding, *Chinese Journal of Chemical Physics*, 2015, **28**, 771–776.
- 6 J. Long, X. Yuan, C. Ma, M. Du, X. Ma, Z. Wen, R. Ma, Y. Wang and Y. Cao, *RSC Advances*, 2018, **8**, 1469–1476.
- 7 L. Luo, R. Liu, Y. Liu, W. Zhuang, Y. Li and T. Gao, *Inorganic Chemistry Communications*, 2020, **118**, 107972.
- 8 S. K. Sharma, S. S. Pitale, M. Manzar Malik, R. N. Dubey and M. S. Qureshi, *Journal of Luminescence*, 2009, **129**, 140–147.
- 9 G. N. Nikhare, S. C. Gedam and S. J. Dhoble, *Luminescence*, 2015, **30**, 163–167.
- 10 W. Piotrowski, K. Trejgis, K. Maciejewska, K. Ledwa, B. Fond and L. Marciniak, *ACS Applied Materials & Interfaces*, 2020, **12**, 44039–44048.
- 11 Z. Wang, X. Luan, G. Ma, J. Chen and Y. Liu, *Journal of Materials Science: Materials in Electronics*, 2021, **32**, 12608–12615.
- 12 Y. Lin, Z. Tang, Z. Zhang and C. W. Nan, *Applied Physics Letters*, 2002, **81**, 996–998.
- 13 J. J. Joos, K. Korthout, L. Amidani, P. Glatzel, D. Poelman and P. F. Smet, *Physical Review Letters*, 2020, **125**, 033001.
- 14 R. Zhong, J. Zhang, X. Zhang, S. Lu and X.-j. Wang, *Applied Physics Letters*, 2006, **88**, 201916.
- 15 H. N. Luitel, T. Watari, T. Torikai and M. Yada, *Optical Materials*, 2009, **31**, 1200–1204.
- 16 S. Zhang, R. Pang, C. Li and Q. Su, *Journal of Luminescence*, 2010, **130**, 2223–2225.
- 17 M. Peng, Z. Pei, G. Hong and Q. Su, *Chemical Physics Letters*, 2003, **371**, 1–6.
- 18 A. Nag and T. R. N. Kutty, *Materials Research Bulletin*, 2004, **39**, 331–342.
- 19 E. Nakazawa, Y. Murazaki and S. Saito, *Journal of Applied Physics*, 2006, **100**, 113113.
- 20 C. G. Van de Walle and J. Neugebauer, *Journal of Applied Physics*, 2004, **95**, 3851–3879.
- 21 C. G. Van de Walle, *Handbook of Materials Modeling: Methods*, Springer Netherlands, 2005, pp. 1877–1888.
- 22 S. Lany and A. Zunger, *Physical Review Letters*, 2007, **98**, 045501.
- 23 S. Lany and A. Zunger, *Physical Review B*, 2008, **78**, 235104.
- 24 S. Lany and A. Zunger, *Modelling and Simulation in Materials Science and Engineering*, 2009, **17**, 084002.
- 25 H.-P. Komsa, T. T. Rantala and A. Pasquarello, *Physical Review B*, 2012, **86**, 045112.
- 26 C. Freysoldt, B. Grabowski, T. Hickel, J. Neugebauer, G. Kresse, A. Janotti and C. G. Van de Walle, *Reviews of Modern Physics*, 2014, **86**, 253–305.

- 27 A. Stoliaroff, N. Barreau, S. Jobic and C. Latouche, *Theoretical Chemistry Accounts*, 2018, **137**, 102.
- 28 A. Stoliaroff, S. Jobic and C. Latouche, *The Journal of Physical Chemistry C*, 2020, **124**, 4363–4368.
- 29 A. Stoliaroff, A. Lecomte, O. Rubel, S. Jobic, X. Zhang, C. Latouche and X. Rocquefelte, *ACS Applied Energy Materials*, 2020, **3**, 2496–2509.
- 30 W. Lafargue-Dit-Hauret, C. Latouche and S. Jobic, *The Journal of Physical Chemistry C*, 2021, **125**, 4267–4276.
- 31 W. Lafargue-Dit-Hauret, R. Schira, C. Latouche and S. Jobic, *Chemistry of Materials*, 2021, **33**, 2984–2992.
- 32 G. Kresse and J. Furthmüller, *Computational Materials Science*, 1996, **6**, 15–50.
- 33 G. Kresse and J. Furthmüller, *Physical Review B*, 1996, **54**, 11169–11186.
- 34 G. Kresse and D. Joubert, *Physical Review B*, 1999, **59**, 1758–1775.
- 35 J. Sun, A. Ruzsinszky and J. Perdew, *Physical Review Letters*, 2015, **115**, 036402.
- 36 J. P. Perdew, M. Ernzerhof and K. Burke, *The Journal of Chemical Physics*, 1996, **105**, 9982–9985.
- 37 E. Péan, J. Vidal, S. Jobic and C. Latouche, *Chemical Physics Letters*, 2017, **671**, 124–130.
- 38 A. Stoliaroff, S. Jobic and C. Latouche, *Journal of Computational Chemistry*, 2018, **39**, 2251–2261.
- 39 T. N. Nadezhina, E. A. Pobedinskaya and N. V. Belov, *Kristallografiya*, 1976, **21**, 826–828.
- 40 N. Zhang, Y.-T. Tsai, M.-H. Fang, C.-G. Ma, A. Lazarowska, S. Mahlik, M. Grinberg, C.-Y. Chiang, W. Zhou, J. G. Lin, J.-F. Lee, J. Zheng, C. Guo and R.-S. Liu, *ACS Applied Materials & Interfaces*, 2017, **9**, 23995–24004.
- 41 D. Dutczak, C. Ronda, T. Jüstel and A. Meijerink, *The Journal of Physical Chemistry A*, 2014, **118**, 1617–1621.
- 42 D. Dutczak, T. Jüstel, C. Ronda and A. Meijerink, *Physical Chemistry Chemical Physics*, 2015, **17**, 15236–15249.
- 43 A. Stoliaroff and C. Latouche, *The Journal of Physical Chemistry C*, 2020, **124**, 8467–8478.
- 44 A. Stoliaroff, S. Jobic and C. Latouche, *Computational Materials Science*, 2019, **168**, 221–228.
- 45 J. D. Cox, D. D. Wagman and V. A. Medvedev, *CODATA key values for thermodynamics*, Hemisphere Pub. Corp., New York, 1989.
- 46 M. W. J. E. Chase, *J. Phys. Chem. Ref. Data, Monograph*, 1998, **9**, 1–1951.
- 47 B. Smets, J. Rutten, G. Hoeks and J. Verlijndonk, *Journal of The Electrochemical Society*, 1989, **136**, 2119.
- 48 W. Minquan, D. Wang and L. Guanglie, *Materials Science and Engineering: B*, 1998, **57**, 18–23.
- 49 K. Kaiya, N. Takahashi, T. Nakamura, T. Matsuzawa, G. M. Smith and P. C. Riedi, *Journal of Luminescence*, 2000, **87-89**, 1073–1075.
- 50 T. Nakamura, K. Kaiya, N. Takahashi, T. Matsuzawa, C. C. Rowlands, t. I. V. Beltran-Lopez, G. M. Smith and P. C. Riedi, *Journal of Materials Chemistry*, 2000, **10**, 2566–2569.
- 51 P. Dorenbos, *Journal of The Electrochemical Society*, 2005, **152**, H107–H110.
- 52 F. Clabau, X. Rocquefelte, S. Jobic, P. Deniard, M.-H. Whangbo, A. Garcia and T. Le Mercier, *Chemistry of Materials*, 2005, **17**, 3904–3912.
- 53 K. Van den Eeckhout, P. F. Smet and D. Poelman, *Materials*, 2010, **3**, 2536–2566.
- 54 V. Vitola, D. Millers, I. Bite, K. Smits and A. Spustaka, *Materials Science and Technology*, 2019, **35**, 1661–1677.
- 55 K. Momma and F. Izumi, *Journal of Applied Crystallography*, 2011, **44**, 1272–1276.